INTERNATIONAL JOURNAL FOR NUMERICAL METHODS IN FLUIDS, VOL. 15, 1361–1381 (1992)

BOUNDARY INTEGRAL/SPECTRAL ELEMENT APPROACHES TO THE NAVIER–STOKES EQUATIONS

J. M. OCCHIALINI*, G. P. MULDOWNEY† AND J. J. L. HIGDON‡

Department of Chemical Engineering, University of Illinois, 1209 W California St, Urbana, IL 61801, U.S.A.

SUMMARY

Numerical algorithms are presented which combine spectral expansions on elemental subdomains with boundary integral formulations for solving viscous flow problems. Three distinct algorithms are described. The first demonstrates the use of spectral elements for the classic boundary integral method for steady Stokes flow. The second extends this algorithm to include domain integrals for solution of the unsteady Navier–Stokes equations. The third algorithm explores the use of boundary integrals as a means of consolidating uncoupled elemental solutions in a domain decomposition approach. Numerical results demonstrating high-order convergence are presented in each case.

KEY WORDS Boundary integral Spectral methods Navier–Stokes

1. INTRODUCTION

In recent years, spectral methods have proven to be a valuable tool in the numerical investigation of fluid dynamics problems. Within this classification, we include not only classic Fourier expansions but also high-order expansions based on orthogonal polynomials. Despite its rather recent development, the literature in this field is quite extensive and a proper review is not possible here. We refer the reader to the review paper by Hussaini and Zang[1] and the monograph by Canuto *et al.*[2] for a proper introduction to the subject. In early work on spectral methods a single expansion was employed over the entire fluid domain—restricting the method to relatively simple geometries. A notable example of this basic approach is the simulation of turbulent transition by Orszag and Kells.[3] To extend spectral methods to a broader range of problems, one may divide the fluid domain into a number of subdomains and employ separate spectral expansions on each domain. This leads to a broad range of algorithms which may be classified as domain decomposition methods. Various algorithms within this class are distinguished by the manner in which the equations are satisfied (e.g. weighted residuals or pointwise collocation) and the manner in which continuity of physical variables is enforced at element borders. Surveys of different strategies may be found in the aforementioned monograph of Canuto *et al.*[2] and in recent conference proceedings such as Canuto and Quarteroni.[4]

Among the various domain decomposition strategies, we are most interested in the method known as *spectral elements* first proposed by Korczak and Patera.[5] This is a *p*-type finite element

* Current address: Air Products, Allentown, PA, U.S.A.
† Current address: Mobil Research and Development Corporation, Paulsboro, NJ, U.S.A.
‡ Author for correspondence.

0271–2091/92/241361–21$15.50

Received 2 December 1991
Revised 1 June 1992

formulation employing orthogonal polynomial bases, typically using Chebyshev or Legendre polynomials. In its first implementation, the method was restricted to rectilinear elements, however the algorithm was easily generalized to isoparametric mapping of the geometry. Maday and Patera[6] give an updated description of this algorithm. Demaret and Deville[7] present an algorithm with features similar to the spectral element method, but based on a collocation solution of the equations with strong enforcement of function continuity at element borders. The spectral element algorithms have successfully combined the high-order convergence rates of spectral methods with the generality of finite element methods to produce a hybrid method of great versatility.

Spectral methods were initially developed for a special class of problems, but later generalized to handle a broad range of applications. Boundary integral methods represent another class of algorithms of quite different character, which have developed in a similar fashion. Boundary integral methods rely on the existence of a fundamental solution to convert a partial differential equation into an integral equation over the boundary of the domain. The essential feature of the method is that there is no need to discretize the interior of the domain. Thus, the dimensionality of the problem is reduced, and the discretized problem has far fewer unknowns than that of a full domain discretization. The drawback is that the linear system representing the discretized equation has a dense matrix as opposed to the sparse banded matrices encountered in many domain methods. On balance, the reduction in the size of the system is more important, and boundary integral techniques have been used with great success. For an overview of the applications of boundary integral methods in solid mechanics, fluid mechanics, geophysics, acoustics and other areas, the reader is directed to the numerous symposia proceedings[8-16] covering this area.

The earliest fluid dynamics application of boundary integral methods was in aerodynamics where so-called panel methods were used for potential flow calculations. Next, Youngren and Acrivos[17] showed that these techniques were effective for studying low Reynolds number viscous flow, and the boundary integral method has since have proven to be the most popular algorithm for the Stokes equations. Higdon[18] reviews some of the efforts in this area, while the monographs of Kim and Karrila[19] and Pozrikidis[20] present extensive developments on this subject.

While the classic boundary integral method is limited to special circumstances such as Stokes flow or potential flow, numerous authors have considered its generalization to the full Navier–Stokes equations. All of these generalizations require some discretization of the entire fluid domain, thus forfeiting the advantage of the classic boundary integral formulation. Nonetheless, in some areas the hybrid boundary integral methods have yielded useful results. In one approach, Bush and Tanner[21] considered the steady inhomogeneous Stokes equations with the inertial terms treated as a pseudo-body-force. With successive iterations, this generates a regular perturbation expansion in Reynolds number. This method is limited to those interior flow problems for which such a perturbation expansion is uniformly valid. In a more general approach, several groups have used a boundary integral formulation with the full unsteady Navier–Stokes equations. Brebbia and Connor[22] and Skerget[23] and Wu[24] and Patterson *et al.*[25] review the efforts of their respective research groups. These authors use a velocity–vorticity approach in which the vorticity is calculated at each time step, and domain integrals and boundary integrals are then evaluated to solve for the fluid velocity. The vorticity transport equation is solved by finite differences, finite elements or via fundamental solution-domain integral techniques. This approach is especially suited to aerodynamics applications where the vorticity is confined to small regions of the flow. Outside these regions a pure boundary integral representation may be used for the potential flow. Other authors, Hebeker,[26] Bannerjee *et al.*[27] and Kakuda and Tosaka,[28] have studied the Navier–Stokes equations using boundary integral

techniques with a primitive variables approach. Additional references for these research groups and others may be found in the conference proceedings mentioned above.[8-16]

The goal of the present effort is to bring together certain useful features of the spectral element method and the boundary integral method to develop new methods for solving viscous flow problems. Section 2 introduces notation and develops the basic formulation. Section 3.1 shows how the spectral element discretization may be employed in a classic boundary integral formulation for Stokes flow, while Section 3.2 extends these concepts to domain integrals and the Navier–Stokes equations. These sections demonstrate the merit of the spectral discretization and indicate how these ideas may be applied to any boundary integral formulation. Section 4 considers the application of boundary integral techniques as a means of consolidating elemental solutions in a domain decomposition approach. The algorithms in this last section are more speculative in nature but indicate an interesting avenue for future work.

2. BASIC FORMULATION

We are interested in techniques for solving the equations governing the flow of an incompressible constant property Newtonian fluid in arbitrary geometries. These are the unsteady Navier–Stokes equations together with the continuity equation

$$\rho\left(\frac{\partial \mathbf{u}}{\partial t}+\mathbf{u}\cdot\nabla\mathbf{u}\right)=-\nabla p+\mu\nabla^2\mathbf{u} \tag{1}$$

$$\nabla\cdot\mathbf{u}=0. \tag{2}$$

The temporal discretization of the equation follows a standard semi-implicit approach with the pressure and viscous terms treated implicitly, and the inertial terms treated explicitly. This yields a linear elliptic equation at each time step and avoids the severe $O(\Delta x^2)$ diffusive stability criterion. The stability constraint will be dictated by a Courant condition of the form $U\Delta x/\Delta t=O(1)$. With first-order time differencing the equations become

$$\left[\frac{1}{\Delta t}\mathbf{u}+\frac{1}{\rho}\nabla p-\nu\nabla^2\mathbf{u}\right]^{n+1}=\left[\frac{1}{\Delta t}\mathbf{u}-\mathbf{u}\cdot\nabla\mathbf{u}\right]^{n}, \tag{3}$$

$$[\nabla\cdot\mathbf{u}]^{n+1}=0. \tag{4}$$

We shall dispense with the superscripts and consider the solution of general elliptic partial differential equations of the form

$$\nabla^2\mathbf{u}-\alpha^2\mathbf{u}=\mathbf{b}+\nabla p, \tag{5}$$

$$\nabla\cdot\mathbf{u}=0. \tag{6}$$

For simplicity, we have absorbed a factor $(\nu\Delta t)^{-1}$ into the coefficient α^2 and absorbed μ^{-1} in the definition of p. The coefficient α^2 and driving force $\mathbf{b}$ for first-order time differencing may be inferred from (3) above. A more common and desirable choice is to employ a second-order Crank–Nicolson formula for the implicit terms and third-order Adams–Bashforth for the explicit terms. This gives

$$\alpha^2=\frac{2}{\nu\Delta t},\qquad \mathbf{b}=-[\alpha^2\mathbf{u}]^n-[-\nabla p+\nabla^2\mathbf{u}]^n$$

$$+\frac{1}{\nu}\left\{\tfrac{23}{6}[\mathbf{u}\cdot\nabla\mathbf{u}]^n-\tfrac{16}{6}[\mathbf{u}\cdot\nabla\mathbf{u}]^{n-1}+\tfrac{5}{6}[\mathbf{u}\cdot\nabla\mathbf{u}]^{n-2}\right\}. \tag{7}$$

The treatment of the pressure term in some algorithms leads to an oscillation when the Crank–Nicolson formula is used. A modified three-term formula which is second-order accurate and damps the oscillations may be used for the implicit terms. This yields

$$\alpha^2 = \frac{12}{7\nu\Delta t}, \qquad \mathbf{b} = -[\alpha^2\mathbf{u}]^n - \tfrac{4}{7}[-\nabla p + \nabla^2\mathbf{u}]^n - \tfrac{1}{7}[-\nabla p + \nabla^2\mathbf{u}]^{n-1}$$

$$+\frac{1}{\nu}\left\{\tfrac{23}{7}[\mathbf{u}\cdot\nabla\mathbf{u}]^n - \tfrac{16}{7}[\mathbf{u}\cdot\nabla\mathbf{u}]^{n-1} + \tfrac{5}{7}[\mathbf{u}\cdot\nabla\mathbf{u}]^{n-2}\right\}. \tag{8}$$

The general elliptic equation (5) and (6) is the starting point for many numerical approaches, whether they be finite differences, finite elements or spectral methods. In the present study, we explore techniques for solving such systems using high-order spectral elements for the spatial discretization. The basic procedure in a spectral element discretization is to divide the domain into a moderate number of *macroelements*, Figure 1. On each element, all variables are defined as high-order expansions of orthogonal polynomials in terms of local variables (ξ, η). When the geometry discretization $\mathbf{x}(\xi, \eta)$ is of the same order as that of the physical variables $\mathbf{u}(\xi, \eta)$, etc., the discretization is called isoparametric. On each element, the local variables (ξ, η) are defined on the square $[-1, 1]$.[2] We define collocation points on this square with reference to the respective orthogonal polynomials. The Gauss–Legendre points (ξ_i, η_j) are a set of points interior to the element where ξ_i and η_j are chosen as the evaluation points for an N point Gauss–Legendre quadrature formula, i.e. the zeroes of the $N+1$ order Legendre polynomial. The Gauss–Legendre–Lobatto points (ξ_i, η_j) are a set of points extending to the boundary of the element corresponding to the $N+1$ point Lobatto quadrature formula. In a similar fashion, one may define the Gauss–Chebyshev points and the Gauss–Chebyshev–Lobatto points. Finally, we define one-dimensional sets of points ζ_i along the sides of each element, where these points may be of Gauss type (interior to the segment) or Lobatto type (including the end points of the segment).

As a general rule, Chebyshev and Legendre polynomial expansions have comparable accuracy in representing arbitrary functions. The Chebyshev polynomials are more desirable for extremely high-order expansions owing to the existence of fast transform algorithms. In the present effort, the order of the expansion is modest (by spectral standards) and matrix multiplies are equally efficient. Legendre polynomial expansions are preferred in some weak formulations, because the unit weight in Gauss–Legendre integration is consistent with the variational statement and eliminates additional quadrature effort. For much of the work presented here, both choices are acceptable and yield comparable results.

With any of the polynomial representations discussed above, the polynomial expansions may be expressed as product Lagrangian interpolants through the respective collocation points. Thus,

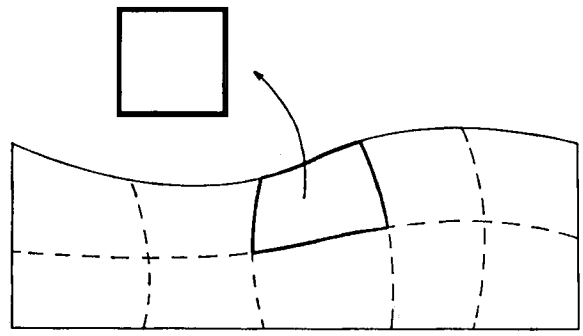

Figure 1. Typical geometry showing macroelement borders in a spectral element discretization

the geometry and all physical variables will be expressed as expansions in the form

$$\mathbf{x}(\xi,\eta)=\sum_{m=1}^{N}\sum_{n=1}^{N}\mathbf{x}_{mn}h_m(\xi)h_n(\eta), \tag{9}$$

where h_m and h_n are Lagrangian interpolants satisfying $h_m(\xi_n)=\delta_{mn}$. Note that different variables may use different bases, e.g. velocity on a Gauss grid and pressure on a Lobatto grid.

In a similar fashion, quantities defined along a boundary of an element may be defined in terms of the one dimensional interpolant

$$f(\zeta)=\sum_{m=1}^{N}f_m h_m(\zeta). \tag{10}$$

In the sections below, we will employ these discretization in a number of algorithms for the solution of the elliptic partial differential equations (5) and (6).

3. BOUNDARY INTEGRAL FORMULATIONS

The boundary integral method (or boundary element method) has proven to be popular in many contexts as discussed in the Introduction. Our goal in this section is to discuss its implementation using the high-order spectral element discretization described in Section 2. We start by considering the implementation for the steady Stokes equations which involves only boundary integrals. We then consider equations of type (5) and (6) which require a domain integral as well.

3.1. Spectral boundary integral method for Stokes equations

The Stokes equations and continuity equation governing incompressible low Reynolds number flow are

$$\nabla\cdot\boldsymbol{\sigma}\equiv-\nabla p+\mu\nabla^2\mathbf{u}=0, \tag{11}$$

$$\nabla\cdot\mathbf{u}=0. \tag{12}$$

Let $\mathbf{u}$, $\boldsymbol{\sigma}$ represent one solution of (11) and (12) and $\mathbf{u}^*$, $\boldsymbol{\sigma}^*$ represent another solution. A fundamental identity for Stokes equations, analogous to Green's identity gives

$$\frac{\partial}{\partial x_j}(u_i\sigma_{ij}^*-u_i^*\sigma_{ij})=0. \tag{13}$$

Choose $\mathbf{u}^*$, $\boldsymbol{\sigma}^*$ to be the velocity and stress associated with the fundamental solution and integrate (13) over the fluid domain to obtain the integral formula

$$u_i(\mathbf{x}_0)=\frac{1}{C\pi\mu}\int_S[S_{ij}(\hat{\mathbf{x}})f_j-T_{ijk}(\hat{\mathbf{x}})u_j n_k]\,\mathrm{d}S. \tag{14}$$

This states that the velocity at a point $\mathbf{x}_0$ may be expressed as a integral of the velocity $\mathbf{u}$ and surface stress $\mathbf{f}\equiv\boldsymbol{\sigma}\cdot\mathbf{n}$ over the boundary of the domain. The vector $\hat{\mathbf{x}}$ is defined as $\mathbf{x}_0-\mathbf{x}$. The constant in front of the integral has value $C=4$ for a point in the interior of the domain, and $C=2$ for a point $\mathbf{x}_0$ on the boundary of the domain. The fundamental solution for two-dimensional Stokes flow is expressed

$$S_{ij}(\hat{\mathbf{x}})=\delta_{ij}\ln r-\frac{\hat{x}_i\hat{x}_j}{r^2}\qquad T_{ijk}(\hat{\mathbf{x}})=4\mu\frac{\hat{x}_i\hat{x}_j\hat{x}_k}{r^4}. \tag{15}$$

Details concerning these equations may be found in Higdon.[18]

In a standard problem, we apply (14) for points $\mathbf{x}_0$ located on the boundary of the domain. Together with the boundary conditions on **u** or **f**, this yields a Fredholm integral equation. The solution of the integral equation provides the remaining boundary values for **u** and **f**. Once the velocity and surface stress are known around the boundary, equation (14) may be used to evaluate interior velocities.

To implement the spectral element version of the boundary integral method, we divide the domain into a moderate number of macroelements as shown in Figure 1. For Stokes flow problems, we require only the discretization of the boundary. Let the geometry $\mathbf{x}(\zeta)$ and the physical variables $\mathbf{u}(\zeta)$ and $\mathbf{f}(\zeta)$ be defined as expansions in terms of the local parametric variable ζ on each segment of the boundary; i.e. as interpolants of the form (10). These expansions may be defined with respect to any of the basis sets described in Section 2; i.e. Gauss–Legendre, Lobatto–Legendre, Gauss–Chebyshev or Lobatto–Chebyshev. It is more convenient to define the surface stress **f** at Gauss points, because **f** is not continuous at corners or at positions where the boundary slope is discontinuous. Choosing Lobatto points for **f** would require double numbering of the nodes at the ends of the segments to accommodate such discontinuities. On the other hand, **u** is continuous over the entire boundary, and the use of Lobatto points is consistent with this continuous dependence. We have successfully implemented the boundary integral algorithm with both Gauss and Lobatto bases for **u**. The results are of comparable accuracy and either choice works equally well.

With the choice of the function bases determined, the next question concerns the discrete form of the integral equation. One may require the equation to be satisfied at discrete collocation points or follow a weighted residuals approach. Owing to the singular form of the kernels, and the resultant quadrature expense, we choose the collocation procedure. As with the function bases, we must then choose between Gauss and Lobatto point distributions. In all cases, Gauss points are preferred because they lie in the interior of the segments. Evaluation of the singular integrals at the ends of the segments is less convenient for two reasons. First, the constant $C=2$ in (14) takes this simple value only for smooth sections of the boundary. If $\mathbf{x}_0$ lies on a corner or at a position of discontinuous slope, C is proportional to the local solid angle subtended by the boundary. Such a choice needlessly complicates the analysis with no offsetting benefit. Second, if the velocity is evaluated at a segment end, extra caution is required to minimize round-off errors when two large numbers of comparable size and opposite sign are added. The use of interior collocation points avoids both of these problems and is the method of choice. Both Gauss–Legendre and Gauss–Chebyshev distributions have been used with equal success.

The implementation of the spectral element discretization is now straightforward. Interpolants (10) are substituted for the respective functions **u** and **f** in (14) and numerical integrations performed for points $\mathbf{x}_0$ located at the Gauss collocation positions. The result is a linear system of algebraic equations

$$\mathbf{u}=\mathbf{A}\mathbf{f}+\mathbf{B}\mathbf{u}. \tag{16}$$

The system matrices **A** and **B** are defined as integrals of the kernels and Lagrangian interpolants over the boundary elements. Each matrix is of order $2NN_E$, where N is the order of the polynomials and N_E is the number of boundary elements. If Lobatto points are used for **u**, then the order of the Lobatto interpolant is $N+1$ to give the same number of unknowns as the N point Gauss basis (owing to the coupling of function values at the endpoints). The matrices **A** and **B** are dense, with elemental submatrices $\mathbf{A}_{\alpha\beta}$ and $\mathbf{B}_{\alpha\beta}$ giving the velocity at points on element α owing to the integrals over element β. The explicit expressions for these submatrices are

$$\mathbf{A}_{\alpha\beta}(m, n)=\frac{1}{2\pi\mu}\int_{-1}^{1}\mathbf{S}[\mathbf{x}_{\alpha_m}, \mathbf{x}_\beta(\zeta)]h_n(\zeta)\omega\,\mathrm{d}\zeta,$$

$$\mathbf{B}_{\alpha\beta}(m,n)=\frac{-1}{2\pi\mu}\int_{-1}^{1}\mathbf{T}[\mathbf{x}_{\alpha_m},\mathbf{x}_\beta(\zeta)]\cdot\mathbf{n}h_n(\zeta)\omega\,\mathrm{d}\zeta, \tag{17}$$

where ω is the differential arc length $\mathrm{d}S/\mathrm{d}\zeta$.

These integrals are evaluated by Gauss–Legendre quadratures with the aid of variable transformations. Briefly, there are four types of integrals which give slow convergence, each requiring a different co-ordinate stretch for efficient quadratures. These special cases are distinguished by the location of ζ^*, defined as the point on the element lying closest to the collocation point: (i) singular integrals with a collocation point on the element $\zeta^*=\zeta_m$; nearly singular integrals with (ii) point of closest approach ζ^* interior to the element, (iii) point ζ^* at end point with collocation point nearly on axis (iv) point ζ^* at end point with collocation point off axis. A comprehensive study of the transformations required in each case are given by Muldowney[29] and Occhialini.[30] With these techniques, integrals have been evaluated with a precision as high as 12 significant figures. Adaptive quadratures are employed with small quadrature counts for the smoothest integrands and as many as 80 points needed for 12-figure accuracy on the most difficult cases.

We have employed the spectral boundary integral method for numerous Stokes flow problems[29,30] involving both rectangular and general curvilinear domains. For problems with smooth solutions, exponential convergence is achieved consistent with the performance of other spectral element methods. Even for non-smooth problems, excellent convergence is achieved. Figure 2 shows the model geometry for a test problem with curved boundaries. We consider a boundary element discretization with $N_E=6$ elements, two along the top and bottom and a single element at each end. Three test cases are considered. In Case I, velocity data is specified at all positions around the boundary. In Case II velocity data is supplied on the top and bottom surfaces, with f_x, u_y specified on the ends. In Case I and II the specified boundary data is taken from a simple parabolic flow $u_x=1-y^2$, $u_y=0$. In other words, the test domain illustrated in Figure 2 is taken as a window on the parabolic flow field. Note that the solution in these problems is non-trivial, because the sinusoidal bottom wall introduces a sinusoidal dependence in the boundary data. In Case III, we specify the same type of boundary conditions as for Case II, but choose $\mathbf{u}=\mathbf{0}$ on the bottom, $u_x=1, u_y=0$ on the top and $f_x=0$, $u_y=0$ on the ends. This corresponds to a flat plate translating above a rigid periodic wall. The boundary element discretization and computation time is identical for all three cases.

Table I shows the performance of the spectral boundary element method for these three test cases. The condition number for the matrices is based on the estimate returned by the Linpack routine DGECO. Case I constitutes an integral equation of the first kind, which is known to lead to an ill conditioned system of equations. Despite the high condition numbers (up to 2×10^5, we find spectral convergence yielding a maximum relative error in $\mathbf{f}$ of $1{\cdot}6\times10^{-7}$ at $N=18$. Note that the error increases somewhat at $N=20$ owing to the presence of round-off errors. Slightly better results might be obtained using more elements; however, with these high condition numbers, it is difficult to achieve more than eight-figure accuracy using double precision arithmetic.

In Case II, we have mixed boundary data and the integral equation cannot be classified as an equation of either the first kind or the second kind. It is interesting that the condition numbers are much smaller in this case even though a major portion of the boundary has the form of a first kind equation. The errors in $\mathbf{f}$ are similar to those of Case I, while the error in $\mathbf{u}$ (calculated on the end boundaries) is smaller by a factor proportional to the condition number.

As a final test, in Case III we have solved for the periodic flow field for a flat plate translating over a rigid wall. Table I shows the convergence of the shear stress at the crest of the wave. The system matrix and condition number are identical to Case II, and we would expect to see the same

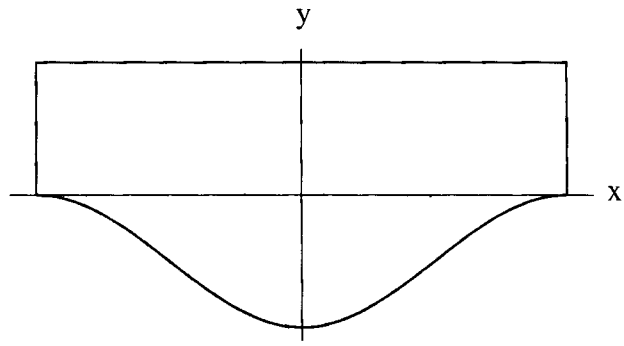

Figure 2. Test geometry for boundary integral solution of Stokes equations. End boundaries at $x = \pm 1$, top boundary at $y = 0.5$, bottom boundary specified by $y = -0.25\,(1 + \cos \pi x)$ yielding a maximum slope of $\pi/4$

Table I. Numerical test results for boundary integral solution of Stokes equations. Test geometry is shown in Figure 2. N is the order of the spectral element representation, N_Q is the number of quadrature points. Computation times (quadratures/matrix factorization) are in seconds on IBM RS 6000/320. Errors listed in Case I and II are maximum over entire domain. Shear stress τ in Case III is evaluated at the crest of the wave, $x = (-1, 0)$.

			Case I		Case II			Case III
N	N_Q	CPU	Condition No.	Error f	Condition No.	Error f	Error u	τ
4	8	0·29/0·01	$1{\cdot}1 \times 10^{3}$	$2{\cdot}1 \times 10^{0}$	$1{\cdot}6 \times 10^{2}$	$5{\cdot}2 \times 10^{-1}$	$2{\cdot}0 \times 10^{-2}$	2·25106342
6	12	0·67/0·04	$4{\cdot}6 \times 10^{3}$	$1{\cdot}5 \times 10^{-1}$	$2{\cdot}5 \times 10^{2}$	$4{\cdot}0 \times 10^{-2}$	$6{\cdot}4 \times 10^{-4}$	2·10403540
8	24	1·74/0·09	$1{\cdot}2 \times 10^{4}$	$4{\cdot}4 \times 10^{-3}$	$3{\cdot}5 \times 10^{2}$	$7{\cdot}8 \times 10^{-4}$	$1{\cdot}0 \times 10^{-5}$	2·10237971
10	40	3·76/0·17	$2{\cdot}4 \times 10^{4}$	$1{\cdot}2 \times 10^{-4}$	$4{\cdot}5 \times 10^{2}$	$1{\cdot}5 \times 10^{-4}$	$2{\cdot}9 \times 10^{-7}$	2·10557399
12	48	5·85/0·30	$4{\cdot}2 \times 10^{4}$	$1{\cdot}9 \times 10^{-5}$	$7{\cdot}8 \times 10^{2}$	$1{\cdot}8 \times 10^{-5}$	$1{\cdot}0 \times 10^{-8}$	2·10557452
14	60	9·17/0·45	$6{\cdot}8 \times 10^{4}$	$3{\cdot}7 \times 10^{-6}$	$1{\cdot}0 \times 10^{3}$	$4{\cdot}4 \times 10^{-6}$	$1{\cdot}9 \times 10^{-9}$	2·10547803
16	72	13·48/0·66	$1{\cdot}0 \times 10^{5}$	$4{\cdot}1 \times 10^{-7}$	$1{\cdot}4 \times 10^{3}$	$4{\cdot}0 \times 10^{-7}$	$2{\cdot}8 \times 10^{-10}$	2·10547503
18	80	18·12/0·93	$1{\cdot}5 \times 10^{5}$	$1{\cdot}6 \times 10^{-7}$	$1{\cdot}8 \times 10^{3}$	$1{\cdot}2 \times 10^{-7}$	$7{\cdot}9 \times 10^{-11}$	2·10547764
20	80	21·63/1·26	$2{\cdot}0 \times 10^{5}$	$6{\cdot}9 \times 10^{-7}$	$2{\cdot}3 \times 10^{3}$	$1{\cdot}6 \times 10^{-7}$	$1{\cdot}2 \times 10^{-10}$	2·10547772

convergence rate. This is borne out in the results where τ has converged to eight significant figures.

The test problems above are typical of the results one may achieve with the spectral boundary element method when the solution is a smooth function. Even when the solution possesses singularities however, this method may be employed with excellent results. Figure 3 shows the streamlines for a model problem involving viscous shear flow over a 3:1 rectangular cavity. The flow is driven by rigid translation of a horizontal plate two cavity widths above the top of the cavity. As is well-known, the surface stress is singular at the top corners of the cavity, and there is an infinite sequence of Moffatt eddies in the lower corners. Table II shows the convergence of shear stress at various locations along the bottom of the cavity. As noted, the convergence rate is excellent at all positions across the cavity.

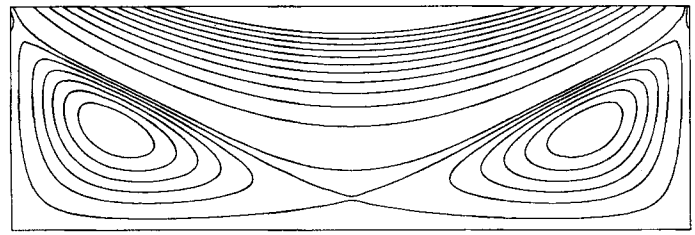

Figure 3. Streamlines for a Stokes shear flow over a rectangular cavity with aspect ratio 3:1

Table II. Dimensionless shear stress along bottom of 3:1 cavity for Stokes flow illustrated in Figure 3. Cavity covers interval $x=[-1, 1]$. Convergence of spectral discretization as a function of expansion order N. Positions x listed correspond to centers of five boundary elements located on cavity bottom.

N	$x=-0{\cdot}900$	$x=-0{\cdot}600$	$x=-0{\cdot}025$	$x=0{\cdot}575$	$x=0{\cdot}900$
5	−0·013636	−0·098014	−0·033863	−0·098188	−0·013627
7	−0·013623	−0·098408	−0·034234	−0·098225	−0·013622
9	−0·013626	−0·098507	−0·034382	−0·098315	−0·013626
11	−0·013626	−0·098554	−0·034456	−0·098357	−0·013626
13	−0·013625	−0·098577	−0·034465	−0·098380	−0·013625

3.2. Spectral boundary integral method for Brinkman's equation

We return now to consideration of the elliptic equation (5) resulting from the time differenced Navier–Stokes equations. This equation is sometimes referred to as Brinkman's equation. In other contexts, it has been employed as a model for flow in porous media with α^2 representing the permeability. To develop an integral formulation for Brinkman's equation, we start by rewriting (5) in terms of the stress tensor σ

$$\nabla\cdot\sigma-\alpha^2\mathbf{u}=\mathbf{b}, \quad \nabla\cdot\mathbf{u}=0. \tag{18}$$

Consider a solution $\mathbf{u}$, σ of the inhomogeneous equation (18) and choose a reference solution $\mathbf{u}^*$, σ^* of the *homogeneous* equation (e.g. with $\mathbf{b}\equiv 0$). The Green's identity for Brinkman's equation gives

$$\frac{\partial}{\partial x_j}(u_i\sigma_{ij}^*-u_i^*\sigma_{ij})=u_i^*b_i. \tag{19}$$

Choosing $\mathbf{u}^*$, σ^* to be the fundamental solution of Brinkman's equation and integrating over the domain yields

$$u_j(\mathbf{x}_0)=\frac{1}{C\pi\mu}\int_{\partial\Omega}[L_{ij}(\hat{\mathbf{x}})f_i-K_{ijk}(\hat{\mathbf{x}})u_in_k]\,\mathrm{d}S+\frac{1}{2C\pi\mu}\int_{\Omega}[L_{ij}(\hat{\mathbf{x}})b_i]\,\mathrm{d}V. \tag{20}$$

The constant $C=2$ for a point in the interior and $C=1$ for a point on the boundary.

The fundamental solution L, K for the two-dimensional Brinkman equation is given by

$$L_{ij}(\hat{x})=-\delta_{ij}\left[K_0(\alpha r)+\frac{K_1(\alpha r)}{(\alpha r)}-\frac{1}{(\alpha r)^2}\right]+\frac{\hat{x}_i\hat{x}_j}{r^2}\left[K_0(\alpha r)+\frac{2K_1(\alpha r)}{(\alpha r)}-\frac{2}{(\alpha r)^2}\right] \tag{21}$$

$$K_{ijk}(\hat{x}) = (\hat{x}_j \delta_{ik}) \left[1 + 2K_0(\alpha r) + \frac{4K_1(\alpha r)}{(\alpha r)} - \frac{4}{(\alpha r)^2} \right] + (\hat{x}_k \delta_{ij} + \hat{x}_i \delta_{jk}) \left[(\alpha r) K_1(\alpha r) + \frac{4K_1(\alpha r)}{(\alpha r)} - \frac{4}{(\alpha r)^2} \right]$$
$$+ \frac{\hat{x}_i \hat{x}_j \hat{x}_k}{r^2} \left[-8K_0(\alpha r) - 2(\alpha r) K_1(\alpha r) - \frac{16K_1(\alpha r)}{(\alpha r)} + \frac{16}{(\alpha r)^2} \right], \tag{22}$$

where K_0 and K_1 are modified Bessel functions.

As before, the integral formula (20) evaluated for points $\mathbf{x}_0$ on the boundary is combined with the boundary conditions on $\mathbf{u}$, $\mathbf{f}$ to yield an integral equation for the unknown boundary values. Velocities may then be evaluated at interior points $\mathbf{x}_0$ in terms of known function values. The most important difference between (14) and (20) is that the latter requires the evaluation of integrals over the entire domain Ω rather than just the boundary $\partial\Omega$ as in (14). In most cases, this will prove to be the most computationally intensive part of the calculation.

In the spectral element implementation, the domain is divided into macroelements as illustrated in Figure 1. Along the boundary of the domain, the geometry and physical variables are discretized in the manner described above for the Stokes equations. The interior of the domain is discretized with product interpolants as defined in (9) using a Gauss–Chebyshev basis. The solution for the velocity field throughout the domain then requires three steps (i) evaluation of the integral formula (20) for points $\mathbf{x}_0$ on the boundary to set-up the boundary integral system; (ii) solution of the linear algebraic system to determine the remaining boundary values and (iii) evaluation of the integrals in (20) to evaluate $\mathbf{u}$ at interior points.

The discretized boundary integral equation for (20) takes the form

$$\mathbf{u} = \mathbf{A}\mathbf{f} + \mathbf{B}\mathbf{u} + \mathbf{u}_\Omega, \tag{23}$$

where the system matrices $\mathbf{A}$ and $\mathbf{B}$ are the same as above (16), but with the Brinkman kernels L and K substituted in place of the Stokes kernels S and T. The techniques for efficient quadrature evaluation are the same and numerous quadrature tests are described by Muldowney.[29] For an independent assessment of the accuracy of the boundary and domain contributions, Muldowney first solved the boundary integral equation for the homogeneous Brinkman equation (with $\mathbf{b}$, and, hence, $\mathbf{u}_\Omega = 0$). For smooth test solutions, exponential convergence was observed with relative errors reaching 10^{-9} for an $N = 20$ expansion. This confirms the accuracy of the quadrature techniques, and demonstrates that the system matrices $\mathbf{A}$ and $\mathbf{B}$ are well-conditioned for Brinkman kernels with spectral discretization.

The next step in the implementation of the boundary integral formulation is the evaluation of the domain integrals to calculate $\mathbf{u}_\Omega$. For points well away from the macroelement of integration, a simple product Gauss–Legendre formula will give good results with modest quadrature counts. Unfortunately for points $\mathbf{x}_0$ on the boundary or in the interior of a given element, the domain integrals have a singular kernel and special steps must be taken to obtain accurate integrations. Briefly, for points on this element, the element is divided into triangular regions as shown in Figure 4. Each of these regions is then mapped to a square, and product Gaussian quadratures applied in the mapped co-ordinates. Product Lagrangian interpolants are used to evaluate $\hat{\mathbf{x}}$ and $\mathbf{b}$ at the quadrature points based on their known values on the elemental grid. This procedure has been used to evaluate domain integrals with relative errors as small as 10^{-12} using quadrature counts as high as 48 points. Muldowney discusses mappings and refinements which can further reduce the quadrature effort. With independent checks on the boundary integral performance and on the accuracy of the domain integrals, the spectral element discretization of the Brinkman integral formula (20) has achieved the accuracy and convergence rates one would expect from a spectral method. The remaining test is to verify its temporal stability in solving the Navier–Stokes equations.

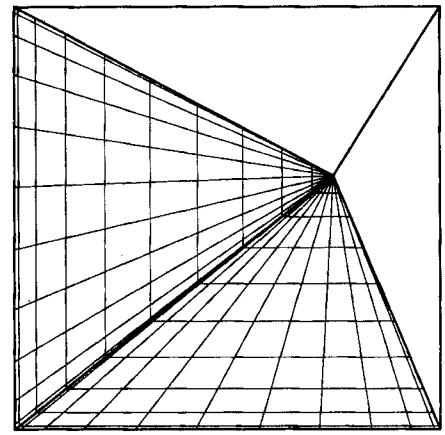

Figure 4. Layout of triangles for subdivision of square and resulting position of quadrature points for singular domain integration by Gaussian quadrature

Given an initial velocity field defined across the fluid domain, the driving force **b** is calculated using differentiation matrices applied to the spectral element discretization. The pressure field is not needed since **b** may be calculated from the velocity and previous values of **b**.[29] (For multistep time formulas such as employed here (7), multiple intial fields are needed.) Given **b** and boundary conditions on **u** and/or **f** the boundary integral equation is solved for boundary values, and interior integrals evaluated to find **u** over the entire domain. The driving force **b** is updated and the calculation proceeds.

The test problem illustrated in Figure 5 is an exact solution of the Navier–Stokes equations due to Kovasznay.[31] The velocity is given by

$$u = u_0 - u_0 e^{\beta x} \cos \pi y, \qquad v = \frac{1}{\pi} u_0 \beta \sin \pi y,$$

$$p = -\tfrac{1}{2} \rho u_0^2 e^{2\beta x}, \qquad \beta = \frac{u_0}{2\nu} - \left[\left(\frac{u_0}{2\nu} \right)^2 + \pi^2 \right]^{1/2}. \tag{24}$$

We have solved this problem on a square $[-1, 1]^2$ and on a mapped element illustrated in Figure 6.

To be more specific, the mapped element is positioned as a window on the Kovasznay flow field with values of velocity or surface stress supplied as boundary conditions. Various tests were performed over a range of Reynolds numbers, time steps, initial fields and boundary conditions. In the first test, the exact solution was specified as the initial field using a high-order expansion. At low Reynolds numbers the initial velocity errors were as small as 10^{-12}. Calculations were then conducted for several hundred time steps (with Δt slightly below the Courant condition) showing negligible growth in the velocity error. Next, calculations were performed at Reynolds numbers of 1, 10 and 100 on a 10×10 grid with increasing time steps. In each case, the relative velocity errors remained unchanged $O(10^{-5})$ after 300 time steps for all Δt less than the Courant limit. Various combinations of force and velocity boundary conditions were tried with stable results in all cases.

To test the sensitivity to initial conditions, calculations were performed using initial data $\mathbf{b} = 0$ which constitutes a rapid start with sharp initial gradients. In each case ($Re = 1$, 10, 100), the

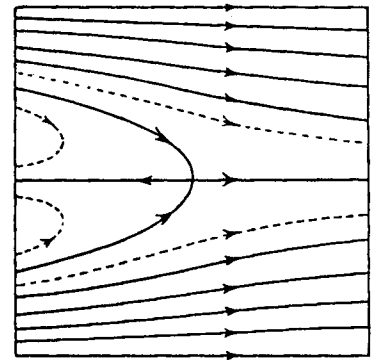

Figure 5. Streamlines for Kovasznay flow given by equation (24)

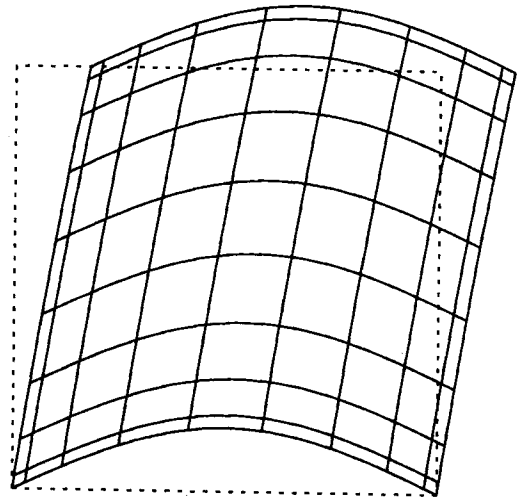

Figure 6. Mapped element for test computations. Mapped variables (ξ, η) defined on square $[-1, 1]^2$. Mapped element defined by $x=(\xi-1)+\exp[k(1+\eta)]$, $y=\eta+2k\cos(1/2\pi\xi)$

velocity errors decayed monotonically over time (50 Δt) in accordance with the appropriate viscous decay rate.

We conclude that the boundary/domain integral formulation leads to a robust, accurate and stable time-stepping algorithm for the solution of the Navier–Stokes equations. The primary concern is efficiency. The three components of the computational effort are the evaluation of the domain integrals, the evaluation of the boundary integrals and the solution of the boundary integral equation. The first component is clearly the largest. If one stores the integrals of the interpolants, the quadrature counts are irrelevant and the domain integrals require an order $2N_\Omega$ matrix multiply each time step where N_Ω is the total number of nodes throughout the domain. There is, however, an $O(4N_\Omega^2)$ storage requirement. On the other hand, if one were looking at massively parallel architectures, one might choose to repeat the quadratures each time step. In this case, the memory and communication requirements are negligible and up to $O(N_E \times N_\Omega)$

processors could be employed with identical instructions. Similar comments apply to the boundary integral evaluations but with proportionately smaller operation counts and storage requirements.

The final computational component is the boundary integral solution. Since this matrix is small, order $2N_{\partial\Omega}$ (number of boundary nodes), its inversion by direct methods is likely to remain an insignificant part of the overall computational load. Nonetheless, this effort might be further reduced by iterative techniques as discussed by Muldowney. In preliminary tests, partial Gaussian elimination was used as a preconditioner with generalized conjugate residual iteration, yielding a fivefold decrease in computation time.

It is clear that the present spectral boundary/domain integral formulation is not competitive with state of the art spectral element algorithms for problems where viscous effects are important throughout the fluid region. It may be of great interest, however, in those applications such as aerodynamics where localized viscous regions border potential flow regions. In such problems, the spectral element discretization may be employed for both the viscous region and for the strict boundary integral solution for the potential flow. One may use either the primitive variable approach considered here or one of the alternative boundary element formulations. We have successfully tested the spectral boundary integral method on a variety of other elliptic equations including Laplace's equation, Poisson's equation and the Helmholtz equation. Compared to low-order methods, spectral element discretization offers significantly higher accuracy with the same number of unknowns. In most spectral methods, this increased accuracy must be balanced against the increased computational cost of the algorithm. In boundary integral implementations, the system matrices are dense, so there is no increase in bandwidth; the quadrature counts are dictated by the singular kernels, so there is little change in the cost of integrations. The spectral boundary integral method, thus, enjoys all of the advantages of other spectral methods with none of the extra costs.

4. BOUNDARY INTEGRAL APPROACH TO SPECTRAL DOMAIN DECOMPOSITION

The development of domain decomposition methods has proven to be an active area of research in recent years. In such an approach, the aim is to solve a number of small local problems independently, and then to consolidate these local representations into a globally continuous solution. Typically, the consolidation phase involves an iterative relaxation method to resolve discontinuities in velocities and stresses. In this section, we discuss the application of boundary integral concepts in this area. We begin by considering a local solution using a standard spectral-order finite element algorithm on a single element, and then show how these solutions may be combined in a global solution.

4.1. Elemental formulation

Consider the set of elliptic equations (5) and (6) defined on an arbitrary quadrilateral element, mapped to local co-ordinates (ξ, η) on the square $[-1, 1]^2$. Define the velocity vector $\mathbf{u}$ on an N point Gauss–Chebyshev–Lobatto grid, and the pressure on a $N-1$ point Gauss–Chebyshev interior grid. For the moment, we assume the Dirichlet conditions are supplied on the boundary of the element for both components of $\mathbf{u}$. The elliptic equations (5) are treated as Helmholtz equations for each velocity component

$$\nabla^2\mathbf{u} - \alpha^2\mathbf{u} = \mathbf{g}, \tag{25}$$

where $\mathbf{g} = \mathbf{b} + \nabla p$.

A variational formulation of the equation (25) requires minimization of the functional

$$I=\int_{\Omega}[-\tfrac{1}{2}\mathbf{Vu}\cdot\mathbf{Vu}-\tfrac{1}{2}\alpha^2u^2-ug]\,\mathrm{d}V \tag{26}$$

over the subspace of u satisfying the Dirichlet conditions on the boundary.

With the spectral element discretization on the Gauss–Chebyshev grid, this yields a linear algebraic system[5]

$$A_{klmn}u_{mn}=B_{klmn}g_{mn}. \tag{27}$$

To satisfy continuity, one might employ a pressure Poisson approach or use a direct continuity constraint. In either case, a weak integral formulation or a collocation procedure may be used. For convenience, we chose the collocation procedure requiring pointwise satisfaction of continuity on the interior Gauss–Chebyshev grid. This leads to a linear system

$$Q_{klmn}u_{mn}=0. \tag{28}$$

The linear systems (27) may be factored to express the velocity in terms of driving force **b**, boundary values of **u** and pressure. Substituting the results into (28) yields a system of equations to be solved for the pressure field. As is well-known,[2] we require two additional constraints, one to specify the arbitrary constant pressure, and the second to eliminate the highest-order *unconstrained* mode. With these constraints, (28) is solved for p, and (27) solved for **u** giving an accurate divergence free solution of (5) and (6). We have implemented these procedures using direct Gaussian elimination for (27) and (28). Owing to the modest number of unknowns on a single element, this represents a reasonable computational effort.

It should be noted that the elemental solution procedure described above is one of many standard spectral formulations which might be employed on an elemental level. The use of direct methods to solve (27) and (28) is not necessarily the most efficient procedure. Detailed discussions of alternative formulations and efficient iterative techniques are given by Canuto *et al.*[2] and Maday and Patera.[6] In the present circumstances, the formulation given provides a simple and reliable elemental solver. At this stage, we emphasize that the local solution for velocity and pressure are only part of the total solution and do not satisfy any global-elliptic boundary value problem. In Section 4.2, we focus on the techniques used to combine such local solutions to produce a globally continuous solution.

4.2. Consolidation of elemental solutions

We suppose that a local solution of (5) and (6) $\mathbf{u}_\alpha$, p_α has been determined on each element α, (where we reserve Greek subscripts to identify elements). Consider the domain which consists of that volume lying inside Ω and outside element volume Ω_α. For the present, let the function **b** be zero over this volume. Applying the Green's identity (19) and integrating over the volume, yields an integral formula similar to (20), but with no domain integral

$$\mathbf{u}_\alpha(\mathbf{x}_0)=\frac{1}{\pi\mu}\int_{\partial\Omega}[\mathbf{Lf}_\alpha-\mathbf{Ku}_\alpha\mathbf{n}]\,\mathrm{dS}-\frac{1}{\pi\mu}\int_{\partial\Omega_\alpha}[\mathbf{Lf}_\alpha-\mathbf{Ku}_\alpha\mathbf{n}]\,\mathrm{d}S, \tag{29}$$

where $\mathbf{x}_0$ is a point on the boundary of the domain $\partial\Omega$.

The integral formula (29) defines a velocity field which is globally continuous and satisfies the homogeneous Brinkman equation outside element α. Combined with the solution $\mathbf{u}_\alpha$, p_α on the interior of element α, it yields a solution over all of Ω which is globally continuous and satisfies the inhomogeneous Brinkman equation inside α. To satisfy the Brinkman equation over the entire

domain we write an integral formula (29) for each element and sum the contributions to produce the global solution

$$\mathbf{u}(\mathbf{x}_0)=\mathbf{u}_{\alpha_0}(\mathbf{x}_0)+\frac{1}{\pi\mu}\int_{\partial\Omega}[\mathbf{Lf}-\mathbf{Kun}]\,dS-\sum_{\alpha=1}^{N_E}\frac{1}{\pi\mu}\int_{\partial\Omega_\alpha}[\mathbf{Lf}_\alpha-\mathbf{Ku}_\alpha\mathbf{n}]\,dS. \tag{30}$$

This expression may be written in an alternative form by summing over all interior segments. On each interior segment S_γ, define $\Delta\mathbf{u}$ and $\Delta\mathbf{f}$ to be the jump in velocity and surface stress between the elemental solutions on the two sides of the segment. The elemental boundary terms in (30) may then be written as segment sums

$$\mathbf{u}(\mathbf{x}_0)=\mathbf{u}_{\alpha_0}(\mathbf{x}_0)+\frac{1}{\pi\mu}\int_{\partial\Omega}[\mathbf{Lf}-\mathbf{Kun}]\,dS-\sum_{\gamma=1}^{N_{SEG}}\frac{1}{\pi\mu}[\mathbf{L}(\Delta\mathbf{f})-\mathbf{K}(\Delta\mathbf{u})\mathbf{un}]\,dS. \tag{31}$$

In the integral formulas (30) and (31), it is understood that $\mathbf{u}_{\alpha_0}(\mathbf{x}_0)$ is the value of the local elemental solution evaluated at the point $\mathbf{x}_0$. These equations are written for a point on the exterior boundary $\partial\Omega$. For a point on an interior elemental boundary, the same expression applies with $\mathbf{u}_{\alpha_0}(\mathbf{x}_0)$ replaced by the average velocity $\frac{1}{2}(\mathbf{u}_\alpha+\mathbf{u}_\beta)$ evaluated from the elemental solutions on the adjoining elements. Details of this derivation are given by Occhialini.[30]

The expression (31) is slightly more convenient because it requires only a single integral over each segment while the direct application of (30) would integrate over every segment twice.

The algorithm for the global solution of (5) and (6) now involves the following steps:

(1) Specify arbitrary Dirichlet data $\mathbf{u}$ and solve for $\mathbf{u}_\alpha$, p_α on every element.
(2) Evaluate (31) to solve for the globally continuous solution at all points on all segments (but not at points interior to elements).
(3) Solve a boundary integral equation to satisfy the boundary conditions and evaluate $\mathbf{u}$ and $\mathbf{f}$ on the boundary $\partial\Omega$.
(4) Evaluate the boundary integral contribution for $\mathbf{u}$ on all interior segments S_γ.
(5) Resolve for velocity interior to elements using complete values for $\mathbf{u}$.

In effect, steps 1 and 2 represent a particular solution of the partial differential equation. Step 3 yields the correct solution on the boundary $\partial\Omega$. Steps 4 and 5 carry this solution to the interior element borders and to element interiors, respectively. Although this algorithm requires two elemental solutions (steps 1 and 5), these are independent for every element and involve a modest number of unknowns.

In principle, the Dirichlet boundary conditions on each element supplied in step 1 can be arbitrary; however, there are two requirements for a successfull computation. The first is that the boundary conditions should not upset the stability of the time-stepping algorithm. The second is that they should lead to a smooth and accurate elemental solution. This means that the boundary conditions should not degrade the exponential convergence rate of the spectral discretization. While this might appear to be a trivial requirement, it turns out to be quite difficult to achieve in practice. A well-known example illustrating this concern is a Poisson's equation on a square, $\nabla^2\phi=1$, with homogeneous boundary condition $\phi=0$. The inhomogeneous term is a constant, the boundary values are zero, the geometry is rectilinear, yet the problem does not possess a smooth solution; ϕ has singular third derivatives at the corners of the square. The reason is that the boundary conditions imply that ϕ_{xx} and ϕ_{yy} are zero on adjacent sides; hence, both are zero at the corner. One can easily specify Dirichlet conditions which are compatible with the equation at the corner, but this merely shifts the singular derivatives to the next higher order. Muldowney[29] discusses the difficulties encountered in determining boundary data which is compatible with the equation and all of its derivatives.

Given the difficulty in finding appropriate conditions for an arbitrary system, one might simply use the values $\mathbf{u}_{\text{old}}$ from a previous time step. In a steady-state problem, the preliminary (step 1) values on elemental borders would converge to the correct values as the solution converged. This would avoid any artificially induced non-smoothness. Unfortunately, the use of old boundary data can induce temporal instability as discussed below. In an attempt to resolve this issue, we considered classic alternatives to the use of Dirichlet conditions. Unfortunately no combination of Dirichlet, Neumann or Robin conditions eliminates the problem if one lacks information on a proper boundary specification.

Another approach to the problem is to dispense with boundary conditions and require additional integral constraints on the system. For example, one might consider a constrained minimization, searching for the solution of (25) which minimizes a functional

$$E(u)=\int_{\Omega_e}(Lu, Lu)\,\mathrm{d}V \tag{32}$$

on each element. Here L is a linear operator whose form affects the character of the solution.

One can easily show that such a condition guarantees a unique solution to the partial differential equation. (Specifically for any $E(u)>0$ when $u\neq 0$). By appropriate choice of the operator L one might force the higher derivatives to decay at a favourable rate guaranteeing smoothness. Furthermore, one might combine these two ideas and look to minimize the function $E(u-u_{\text{old}})$. We have tested various forms of this minimization condition with mixed results. Detailed tests are described below using u_{old}, $E(u)$ and $E(u-u_{\text{old}})$. After some experimentation, we chose an operator based on scaling arguments, giving

$$E(u)=\int_{\Omega_e}\left[(u)^2+\frac{1}{\lambda^2}(u_\xi^2+u_\eta^2)+\cdots+\frac{1}{\lambda^{2n}n!}(u_{\xi^n}^2+u_{\eta^n}^2)\right]\mathrm{d}V, \tag{33}$$

where λ is a parameter $O(1/\alpha)$.

To test the overall performance of the domain decomposition algorithm outlined in steps 1–5, we consider a Kovasznay flow (24) with various combinations of force and velocity boundary conditions on two domains: a square $[0, 1]^2$ and a mapped domain illustrated in Figure 7.

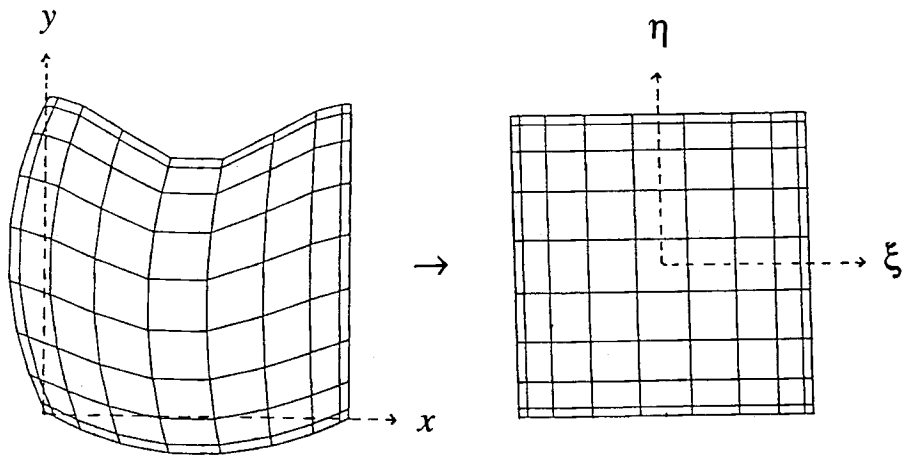

Figure 7. Mapped element for test computations. Top: $x=(1+\zeta)/2$, $y=0.90-0.10\cos(\pi\zeta)$; right: $x=1$, $y=(1+\zeta)/2$; bottom: $x=(1+\zeta)/2$, $y=(\zeta^2-1)/8$; left: $x=(\zeta^2-1)/8$, $y=(1+\zeta)/2$

Table III shows the performance on the square domain with 2, 4 or 9 elements. The boundary conditions specify the velocity u_x and u_y at inlet and outlet, and surface stress f_x and f_y on the top and bottom of the square. The convergence rate is consistent with expectations for a spectral representation (e.g. $O(10^6)$ reduction in error from $N=6$ to $N=12$). Table IV shows comparable results for a mapped domain. Table V shows that the method may be employed with quite arbitrary combinations of boundary conditions, yielding similar accuracy in all cases.

All of the results presented in Tables III–IV are for particular boundary conditions (in step 1) using Dirichlet specifications with $\mathbf{u}=\mathbf{u}_{\text{old}}$. For some combinations of boundary conditions on the mapped domains (Table V), this specification lead to an unstable solution. The source of the instability is as follows. Given a particular boundary condition $\mathbf{u}_{\text{old}}$, one calculates an elemental solution and differentiates to calculate a surface stress. For fixed driving force $\mathbf{b}$, this relates the stresses on the boundary of the element to the velocities via some matrix $\mathbf{M}_1$, where $\mathbf{f}=\mathbf{M}_1\mathbf{u}$. The elemental surface stress enters the boundary integral equation (30) or (31) from which one calculates a new boundary velocity $\mathbf{u}$. Thus, if one has force boundary conditions, the boundary integral solution relates the boundary velocities to the surface stresses though some matrix $\mathbf{M}_2$, $\mathbf{u}=\mathbf{M}_2\mathbf{f}$. The net result is that a new velocity is calculated as $\mathbf{u}_{\text{new}}=\mathbf{M}_2\,\mathbf{M}_1\mathbf{u}_{\text{old}}$. If one has a single consistent representation for velocities and stresses, then $\mathbf{M}_2$ is exactly the inverse of $\mathbf{M}_1$ and the solution will converge if $\mathbf{b}$ has converged. Unfortunately, the discrete matrices $\mathbf{M}_1$ and $\mathbf{M}_2$ are not exactly inverses—$\mathbf{M}_1$ is based on a polynomial approximation to a variational formulation, while $\mathbf{M}_2$ is based on integrals of fundamental solutions. For some cases, involving mapped elements and numerous force boundary conditions, the product $\mathbf{M}_2\mathbf{M}_1$ has eigenvalues greater than 1 leading to instability. In this instability, the driving force $\mathbf{b}$ remains constant, but the homogeneous eigensolution grows exponentially. This problem may be overcome by employing a relaxation parameter, in effect using an average of $\mathbf{u}_{\text{old}}$ from previous time steps. Certain of the results in Table V with force boundary specifications used such a relaxation factor.

Table III. Maximum error in velocity and pressure for Kovasznay flow on square domain as a function of expansion order N for 2, 4 or 9 elements. All results are for Reynolds number $Re=2$, except 9 element results which are for $Re=20$.

N_E	N	u_x	u_y	p
2	6	$2{\cdot}00\times10^{-3}$	$8{\cdot}53\times10^{-4}$	$2{\cdot}23\times10^{-2}$
	7	$1{\cdot}33\times10^{-4}$	$9{\cdot}34\times10^{-5}$	3.26×10^{-3}
	8	$9{\cdot}09\times10^{-5}$	$2{\cdot}09\times10^{-5}$	$8{\cdot}76\times10^{-4}$
	9	$2{\cdot}44\times10^{-6}$	$8{\cdot}83\times10^{-7}$	$7{\cdot}44\times10^{-5}$
	10	$2{\cdot}46\times10^{-6}$	$4{\cdot}49\times10^{-7}$	$2{\cdot}95\times10^{-5}$
	11	$4{\cdot}16\times10^{-8}$	$9{\cdot}00\times10^{-9}$	$1{\cdot}35\times19^{-6}$
	12	$4{\cdot}32\times10^{-8}$	$8{\cdot}39\times10^{-9}$	$7{\cdot}25\times10^{-7}$
4	4	$1{\cdot}50\times10^{-2}$	$1{\cdot}08\times10^{-2}$	$9{\cdot}51\times10^{-2}$
	5	$1{\cdot}21\times10^{-3}$	$5{\cdot}72\times10^{-4}$	$7{\cdot}33\times10^{-3}$
	6	$2{\cdot}19\times10^{-4}$	$6{\cdot}39\times10^{-5}$	$1{\cdot}90\times10^{-3}$
	7	$4{\cdot}84\times10^{-6}$	$2{\cdot}75\times10^{-6}$	$6{\cdot}01\times10^{-5}$
	8	$2{\cdot}46\times10^{-6}$	$5{\cdot}92\times10^{-7}$	$3{\cdot}05\times10^{-5}$
	9	$2{\cdot}53\times10^{-8}$	$2{\cdot}05\times10^{-8}$	$4{\cdot}84\times10^{-7}$
	10	$1{\cdot}52\times10^{-9}$	$9{\cdot}17\times10^{-10}$	$3{\cdot}31\times10^{-8}$
	11	$8{\cdot}53\times10^{-11}$	$2{\cdot}46\times10^{-11}$	$2{\cdot}12\times10^{-9}$
	12	$7{\cdot}36\times10^{-11}$	$1{\cdot}34\times10^{-11}$	$3{\cdot}26\times10^{-9}$
9	8	$3{\cdot}19\times10^{-7}$	$7{\cdot}34\times10^{-8}$	$4{\cdot}43\times10^{-6}$

Table IV. Maximum error in velocity and pressure for Kovasznay flow on mapped domain of Figure 7 as a function of expansion order N for 1, 2 or 4 elements. All results are for Reynolds number $Re = 2$. Results for 2 and 4 elements used a relaxation procedure with boundary data.

N_E	N	u_x	u_y	p
1	4	$1{\cdot}20 \times 10^{-1}$	$1{\cdot}10 \times 10^{-1}$	$1{\cdot}06 \times 10^{+00}$
	6	$4{\cdot}90 \times 10^{-2}$	$4{\cdot}80 \times 10^{-2}$	$5{\cdot}85 \times 10^{-1}$
	8	$6{\cdot}15 \times 10^{-3}$	$6{\cdot}48 \times 10^{-3}$	$9{\cdot}23 \times 10^{-2}$
	10	$8{\cdot}50 \times 10^{-4}$	$4{\cdot}50 \times 10^{-4}$	$1{\cdot}88 \times 10^{-2}$
	12	$1{\cdot}96 \times 10^{-4}$	$1{\cdot}20 \times 10^{-4}$	$7{\cdot}55 \times 10^{-3}$
	14	$2{\cdot}86 \times 10^{-5}$	$2{\cdot}03 \times 10^{-5}$	$1{\cdot}62 \times 10^{-3}$
2	8	$3{\cdot}29 \times 10^{-2}$	$5{\cdot}86 \times 10^{-2}$	$1{\cdot}59 \times 10^{+00}$
	10	$5{\cdot}67 \times 10^{-4}$	$5{\cdot}35 \times 10^{-4}$	$2{\cdot}79 \times 10^{-2}$
	12	$8{\cdot}91 \times 10^{-5}$	$1{\cdot}08 \times 10^{-4}$	$5{\cdot}20 \times 10^{-3}$
4	4	$2{\cdot}76 \times 10^{-2}$	$8{\cdot}63 \times 10^{-2}$	$4{\cdot}88 \times 10^{+00}$
	6	$1{\cdot}25 \times 10^{-2}$	$6{\cdot}10 \times 10^{-3}$	$1{\cdot}06 \times 10^{-1}$
	8	$4{\cdot}53 \times 10^{-5}$	$4{\cdot}60 \times 10^{-5}$	$3{\cdot}06 \times 10^{-3}$
	10	$2{\cdot}64 \times 10^{-6}$	$3{\cdot}27 \times 10^{-6}$	$1{\cdot}60 \times 10^{-4}$
	12	$4{\cdot}26 \times 10^{-7}$	$2{\cdot}25 \times 10^{-7}$	$2{\cdot}31 \times 10^{-5}$

Table V. Maximum error in velocity and pressure for Kovasznay flow on mapped domain of Figure 7 showing effect of different boundary conditions. All results are for Reynolds number $Re = 2$ with $N_E = 4$ and $N = 10$. Boundary condition types are listed in clockwise order around domain: left, top, right, bottom. Boundary condition specification according to type is as follows: (1) $u_x u_y$, (2) $f_x f_y$, (3) $u_x f_y$, (4) $f_x u_y$.

BC	u_x	u_y	p
2111	$2{\cdot}81 \times 10^{-6}$	$3{\cdot}02 \times 10^{-6}$	$2{\cdot}14 \times 10^{-4}$
1221	$6{\cdot}58 \times 10^{-6}$	$4{\cdot}17 \times 10^{-6}$	$2{\cdot}47 \times 10^{-4}$
1222	$7{\cdot}06 \times 10^{-6}$	$7{\cdot}84 \times 10^{-6}$	$2{\cdot}54 \times 10^{-4}$
3414	$3{\cdot}49 \times 10^{-6}$	$2{\cdot}29 \times 10^{-6}$	$1{\cdot}32 \times 10^{-4}$
1422	$5{\cdot}96 \times 10^{-6}$	$3{\cdot}07 \times 10^{-6}$	$1{\cdot}26 \times 10^{-4}$
2234	$4{\cdot}74 \times 10^{-5}$	$3{\cdot}14 \times 10^{-5}$	$3{\cdot}25 \times 10^{-4}$
2121	$2{\cdot}64 \times 10^{-6}$	$3{\cdot}27 \times 10^{-6}$	$1{\cdot}60 \times 10^{-4}$

In an effort to eliminate this eigenmode instability, we conducted tests using the minimization constraint $E(u)$ described above. This completely eliminates the instability, because the particular solution uses no boundary data from the previous time step. Unfortunately, the choice for E given above (33) is not completely successful in producing a smooth particular solution. In general, the errors using the minimization constraint were $O(10^2)$ higher than those using $\mathbf{u}_{old}$ with the same grid. Tests with a minimization constraint based on $E(u - u_{old})$ achieved accuracy comparable to the Dirichlet conditions using $\mathbf{u}_{old}$ and were more stable; however, they still suffered a weak eigenmode instability in the more extreme cases.

In addition to the eigenmode instability, the boundary conditions required for the particular solution introduce a second, more serious instability. It is well-known that virtually any method

employed to solve the time-dependent Navier–Stokes equations will become unstable if the level of discretization is insufficient to resolve the fine details of the flow field. In the present circumstances, the lack of proper boundary conditions for the Helmholtz equations leads to local boundary layers with length scale $O(1/\alpha)$ in the elemental particular solutions. In principle, these boundary layers are removed from the consolidated solution by the segment integrals of equation (31). Unfortunately, if these artificial local boundary layers are not fully resolved by the elemental solution, they are not entirely removed and trigger the instability associated with inadequate resolution.

The condition for resolving the local boundary layers is roughly, $\alpha^2(\Delta x)^2 < O(1)$, i.e. $(\Delta x)^2/\nu\Delta t < O(1)$. This means that the time step Δt must be *greater* than the explicit criteria, while remaining smaller than the Courant limit. For flows at moderate to high Reynolds number, the explicit limit might well approach the Courant limit, leaving no stable time step size. The only course of action is to increase the resolution, reducing the explicit limit $O(\Delta x^2)$ below the Courant limit $O(\Delta x)$. The extra resolution is needed only for the artificial elemental boundary layers not for the actual details of the fluid motion. This constraint makes the current implementation too costly for even modest Reynolds number flows. The Kovasznay flow at Reynolds number 20 was stable only on the 9 element grid of Table IV. While we have accurately calculated flows with slightly higher Reynolds numbers ($Re = 50$), they required still more elements. It is worth emphasizing that the cause of this instability is well-documented and is *not* related to any dominance of inertial terms. In fact, each of the accurate, stable computations ($Re = 2$) in Table IV can be rendered unstable by choosing a sufficiently small time step.

We conclude that the specification of compatible boundary conditions for the elemental particular solutions is of critical importance for the success of the approach. Without such conditions, the algorithm suffers from temporal instabilities which severely limit its range of application. The problem for the applied mathematician may be stated in succinct form: given a constrained elliptic system (5) and (6) defined on a mapped quadrilateral element with smooth geometry $\mathbf{x}(\xi, \eta)$ and smooth driving force $\mathbf{b}$, can one find boundary specifications or other constraints leading to a smooth unique solution. In this context, we mean that $\mathbf{u}$ have the same degree of smoothness as the other functions, i.e. $\mathbf{b}, \mathbf{x} \in C^{(n)}$ guarantees $\mathbf{u} \in C^{(n)}$. A solution to this problem would eliminate the instabilities described above and lead to a robust algorithm for arbitrary domains.

Before closing it is worth noting the potential benefits of the domain decomposition algorithm to motivate further effort in this area. The elemental solutions required in steps 1 and 5 may be accomplished through fast preconditioned iterative solution techniques. As noted previously, such techniques have already been demonstrated for both two- and three-dimensional flows. Because the elemental problems are independent, these solutions may be executed in parallel with no inter-element communication. Further, the small size of the elemental problems leads to modest operation counts and rapid convergence of the iterative solution.

The consolidation integrals ΣS_γ in (31) would be the next major computational effort. In three dimensions, the consolidation integrals require two-dimensional integration over the boundary surfaces of each element—an immense computational burden. In fact, such an assessment ignores the character of the fundamental solutions L and K. These kernels involve Bessel functions in two dimensions and exponentials $\exp(-\alpha r)/r$ in three dimensions. The full kernel, however, is needed only in the near field over distances $O(1/\alpha)$. This distance is typically a small fraction of the element size. Thus, the evaluation of surface integrals would be required only for a small number of nodes on elements immediately adjacent to the given surface. In the far field, the velocity associated with L and K is a potential flow. The leading term is a potential dipole decaying as r^{-3} in three-dimensional flows. Including the first n moments yields expressions accurate to

$O(r^{-(3+n)})$. This expansion would give excellent accuracy on all elements except those bordering the given element. The operation count scales like $N_\Omega \times N_E \times n$, where N_Ω is the totaf number of nodes in the domain, N_E is the number of elements and n is the number of moments included in the far-field potential flow. Given the extremely rapid decay of higher moments, typical values for n might be of order four or five. Again, the computations for each element are completely independent and may be executed in parallel with no communication.

The remaining contribution to the computational effort is the boundary integral solution for the velocities and stresses on the domain boundary. The construction of the boundary integral matrix involves elemental surface integrals with the same near-field/far-field behaviour discussed above. The inversion of the boundary integral system involves a matrix with only $O(N_{\partial\Omega})$ unknowns. Based on the preliminary tests of Muldowney for two-dimensional flows, it appears that these systems might be solved via preconditioned iterative methods. In fact, the iterative methods should be more effective for three dimensions owing to the more rapid far-field decay (r^{-3} versus r^{-2}). This is an issue which merits further consideration.

These brief comments provide only a bare outline for extension of our efforts to large scale three-dimensional simulations. We offer them to indicate the potential of the boundary integral/domain decomposition approach and to stimulate further interest in this area.

5. CONCLUSION

In this paper, we have documented the application of spectral element discretization in three versions of the boundary integral method. For standard algorithms involving strictly boundary integrals, the development in Section 3.1 demonstrates that spectral techniques provide a powerful and efficient algorithm which is easily adaptable to any of the classic equations. For those applications which are amenable to boundary/domain integral formulations, the results of Section 3.2 show that spectral elements are equally well-suited to these algorithms. The spectral discretization may be implemented with primitive variable as in this paper, or with any of the alternative formulations. The final application presented in Section 4 describes an attempt to employ boundary integral techniques in a domain decomposition algorithm for the Navier–Stokes equations. While this last method has been successfully demonstrated on some modest test problems, the present implementation suffers from severe stability limitations. If the problem concerning proper boundary conditions in the particular step can be resolved, this last approach has significant potential for large-scale computations in complex fluid flows.

ACKNOWLEDGEMENTS

This work was supported by the National Science Foundation. G. P. Muldowney received fellowship support from the Fannie and John Hertz Foundation.

REFERENCES

1. M. Y. Hussaini and T. A. Zang, 'Spectral methods in fluid dynamics', *Ann. Rev. Fluid Mech.*, **19**, 339–367 (1987).
2. C. Canuto, M. Y. Hussaini, A. Quarteroni, and T. A. Zang, *Spectral Methods in Fluid Dynamics* Springer, New York, 1988.
3. S. A. Orszag and L. C. Kells, 'Transition to turbulence in plane Poiseulle flow and plane Couette flow', *J. Fluid Mech.*, **96**, 159–205 (1980).
4. C. Canuto and A. Quarteroni, *Spectral and High Order Methods for Partial Differential Equations*, North-Holland, Elsevier, New York, 1990.
5. K. Z. Korczak and A. T. Patera, 'Isoparametric method for solution of the Navier–Stokes equations in complex geometry', *J. Comput. Phys.*, **62**, 361–382 (1986).

6. Y. Maday and A. T. Patera, 'Spectral element methods for the incompressible Navier–Stokes equations', in A. K. Noor and J. T. Oden (eds), *State of the Art Surveys on Computational Mechanics*, ASME, New York, 1989.
7. P. Demaret and M. O. Deville, 'Chebyshev collocation solutions of the Navier–Stokes equations using multi-domain decomposition and finite element preconditioning', *J. Comput. Phys.*, **95**, 359–386 (1991).
8. P. K. Bannerjee and R. P. Shaw, *Developments in Boundary Element Methods–2*, Applied Science, London, 1982.
9. C. A. Brebbia, *Boundary Elements VI, Proc. 6th Int. Conf.* Southampton to New York, Springer, Berlin, 1984.
10. C. A. Brebbia and G. Maier, *Boundary Elements VII, Proc. 7th Int. Conf.*, Villa Olmo, Lake Como, Italy, Springer, Berlin, 1985.
11. M. Tanaka and C. A. Brebbia, *Boundary Elements VIII, Proc. 8th Int. Conf.*, Tokyo, Japan, Springer, Berlin, 1986.
12. C. A. Brebbia, W. L. Wendland and G. Kuhn, *Boundary Elements IX*, Springer, Berlin, 1987.
13. J. J. Connor and C. A. Brebbia, *Betech 86, Proc. 2nd Boundary Element Technology Conf.*, MIT, USA, June 1986, Computational Mechanics, 1986.
14. T. A. Cruse, *Advanced Boundary Element Methods, Proc. IUTAM Symposium*, San Antonio, Texas, 1987, Springer, Berlin, 1987.
15. C. A. Brebbia, *Topics in Boundary Element Research*, Springer, Berlin 1989.
16. B. S. Annigeri and K. Tseng, *Boundary Element Methods in Engineering, Proceedings of the International Symposium on Boundary Element Methods*, East Hartford, CO, Springer, Berlin, 1989.
17. G. K. Youngren and A. Acrivos, 'Stokes flow past a particle of arbitrary shape: a numerical method of solution', *J. Fluid Mech.*, **69**, 377–403 (1975).
18. J. J. L. Higdon, 'Stokes flow in arbitrary two-dimensional domains: shear flow over ridges and cavities', *J. Fluid Mech.*, **159**, 195–226. (1985).
19. S. Kim and S. J. Karrila, *Microhydrodynamics, Principles and Selected Applications*, Butterworth-Heinemann, Boston, 1991.
20. C. Pozrikidis, *Boundary Integral and Singularity Methods for Linearized Viscous Flow*, Cambridge, Cambridge, 1991.
21. M. B. Bush and R. I. Tanner, 'Numerical solution of viscous flows using integral equation methods', *Int. j. numer. methods fluids*, **3**, 71–92 (1983).
22. C. A. Brebbia and J. J. Connor, 'Boundary element formulation for viscous compressible flow', in Ref. 15 (1989).
23. P. Skerget, A. Alujevic, C. A. Brebbia and G. Kuhn, 'Natural and forced convection simulation using the velocity vorticity approach', in Ref. 15 (1989).
24. J. C. Wu, 'Linkage between potential and viscous flows', in Ref. 16 (1989).
25. M. T. Patterson, J. C. Wu and C. M. Wang, 'Boundary element methods for the Navier–Stokes equations', in Ref. 16 (1989).
26. F. K. Hebeker, 'A boundary element spectral element method for nonstationary Navier–Stokes flows', in J. R. Whitman, (ed.), *MAFELAP 1987*, Academic Press, New York, 1988.
27. P. K. Bannerjee, G. F. Dargush, and K. Honkala, 'Advanced boundary element methods for incompressible thermoviscous flow', in Ref. 16 (1989).
28. K. Kakuda and N. Tosaka 'Boundary element analysis of viscous fluid flow problems using the time splitting method', in Ref. 16 (1989).
29. G. P. Muldowney, *Ph.D. Dissertation*, University of Illinois, 1989.
30. J. M. Occhialini, *Ph.D. Dissertation*, University of Illinois, 1991.
31. L. S. G. Kovasznay, 'Laminar flow behind a two dimensional grid', *Proc. Camb. Phil. Soc.*, **44**, 58–62 (1948).